Egyptian Journal of Pure and Applied Science

Modified Coprecipitated Copper Ferrite Nanoparticles as a Dual-Agent for Pb^{2+} and Cd^{2+} Ions Removal and Antibacterial Treatment in Wastewater

Sara Essam [1*], Dina Salah [1], Mohamed A. Hassan [2,3], Ibrahim Hassan [1]

[1] *Physics department, Faculty of Science, Ain Shams University, Cairo, Egypt.*

[2] *Regional Center for Food and Feed, Agricultural Research Center, Giza, Egypt.*

[3] *Nanotechnology and Advanced Materials Central Lab. (NAMCL), Agricultural Research Center, Giza, Egypt.*

A B S T R A C T

Utilizing a modified co-precipitation technique, this study presents the synthesis and comprehensive characterization of Copper Ferrite Nanoparticles (CFNPs). CFNPs, exhibiting an 85.027 m^2/g surface area, 15 nm average particle size, and saturation magnetization (Ms) of 52.68 emu/g, were synthesized utilizing various characterization techniques, including Raman spectroscopy, X-ray diffraction (XRD), Fourier-transform infrared spectroscopy (FT-IR), field emission scanning electron microscopy (FE-SEM), high-resolution transmission electron microscopy (HR-TEM), selected area electron diffraction (SAED), energy-dispersive X-ray spectroscopy (EDX), vibrating sample magnetometry (VSM), Brunauer-Emmett-Teller (BET) analysis, and zeta potential measurement. Adsorption studies focusing on Pb^{2+} and Cd^{2+} ions elucidated maximal capacities of 210.58 mg/g and 149.99 mg/g, respectively, employing Langmuir models. Kinetic analyses supported the pseudo-first-order model, with equilibrium adsorption data aligning well with the Dubinin-Radushkevich isotherm model, highlighting CFNPs' high affinity for heavy metal ions. Furthermore, CFNPs exhibited potent antibacterial efficacy against gram-positive (S. aureus, S. pyrogenous) and gram-negative (E. coli, P. aeruginosa) bacteria, underscoring their multifunctional potential in water remediation and antibacterial applications. This comprehensive investigation offers promising avenues for the environmental and biomedical utilization of CFNPs.

1. Introduction

Life on Earth relies on several basic ingredients, but water is one of the most crucial compounds. Sanitation, human consumption, industrial processes, pharmaceutical production, and agricultural uses are just a few of the many ways water is put to beneficial use. Humans can only make use of less than 3% of the water on Earth. Wastewater in the ground and waterways accounts for the remaining 99.7 % [1]. To increase the amount of water that can be used, water remediation is necessary. Water and waste products from a variety of sources, including homes, medical facilities, factories, and other commercial and industrial operations, all end up in the environment as wastewater [2].

Heavy metal ions have gained significant attention as a major eco-toxicological factor due to the potential harm they cause when their levels exceed toxicity thresholds. Mercury (Hg), cadmium (Cd), arsenic (As), chromium (Cr), thallium (Tl), zinc (Zn), nickel (Ni), copper (Cu), and lead (Pb) are all examples of heavy metals. They have densities between 3.5 and 7 g/cm^3 and are dangerous or poisonous at low doses; also, These metals are non-biodegradable by nature and are abundantly distributed in the crust of the Earth [3]. Common heavy metal pollution sources include sewage sludge, pesticides, ferrous ores, fertilizers, municipal trash, and fossil fuel combustion [4]. Air, water, and food all play a role in introducing them into the human body.

In extremely minute quantities, some play an important function in human and animal metabolism, but in larger quantities, they can be harmful. Lead (Pb^{2+}) and cadmium (Cd^{2+}) ions are two examples of heavy metals that are harmful to humans and aquatic life [5]. Renal failure, hypertension, lung cancer, and osteomalacia are some of the effects of chronic exposure to harmful amounts of Cd^{2+} in humans and animals. At high quantities, Pb^{2+} is toxic to the neurological system and the digestive tract [3]. According to the World Health Organization (WHO), the maximum allowable levels of Pb^{2+} and Cd^{2+} in drinking water are 0.01 mg/L and 0.003 mg/L, respectively [6]. Diseases spread by wastewater are not only caused by the heavy metal ions in it but also by the bacterial communities that bio-contaminate the water.

Contaminations and sever diseases are linked to high concentrations of Gram-positive bacteria such as S. aureus and S. pyrogenous, as well as gram-negative bacteria such as E.Coli and P.aeruginosa, which have been studied extensively as model organisms because of their well-characterized cell walls many contaminations. Therefore, Rising bacteria concentrations in potable water pose serious health risks that are challenging to mitigate [7]. More than 35,000 persons in the United States lose their lives each year due to infections caused by multidrug-resistant (MDR) bacterial diseases [8]. That's why it's crucial to use the right technique for disinfecting water and removing harmful metal ions and dangerous bacteria.

Multiple Water remediation strategies, including flocculation and coagulation [9], photocatalysis [10], ion exchange [11], adsorption [12], membrane filtration [13], and chemical precipitation [14], have been developed by scientists in response to the increased toxic metals contamination. Despite their usefulness in cleaning up wastewater, these methods have certain limitations on their efficacy, including expensive costs, complex processes, long processing times, and low efficiency. The adsorption method was deemed the most effective technology for removing heavy metals from wastewater since it is safe, clean, efficient, and technically possible [15].

Nanoparticles (NPs) have interesting characteristics that make them applicable in many different fields because of their small size. There is strong evidence that these nanomaterials of varying geometries are effective at removing heavy metals [17]. They can bind ions, isolate from pure water, and increase adsorption capacity due to their wide surface area, high porosity, low specific surface charge, and high surface functionality [18]. Zeolites, carbonates, polymers, chitosan, ferrite, apatite, apatite, magnetic oxide, metal oxide, bimetallic metals, metallic materials, and many more have all been used as nanomaterials for wastewater treatment in recent years to remove heavy metals and harmful bacteria [16-19]. There are several categories of advanced nanomaterials, but magnetic nanomaterials stand out as the most useful. As their sizes are reduced to the nanoscale, the materials' properties undergo dramatic transformations. Non-magnetic nanoparticles are less effective in water treatment due to their low surface area and difficulties separating [20].

However, magnetic nanoparticles are safe to use, display no signs of reactive chemical behaviour, and have a sizable surface area, all of which contribute to their widespread distribution. This demonstrates that heavy metals can be efficiently removed by using these nanoparticles [20]. To remove harmful metals from water, various magnetic nanocomposites based on metal oxides have been developed and put to use [21]. Magnetic nanoparticles called metal ferrite were created when ferrite molecules were joined with various metals by the research group. In the case of metal nanocomposites, the typical formula is $M(Fe_xO_y)$, where M is the elemental metal. There are a variety of metal ferrites available for recycling metals, such as $ZnFe_2O_4$, $CuFe_2O_4$, and $Mn_{0.67}Zn_{0.33}Fe_2O_4$ [22–24].

CFNPs have a spinel structure characterized by a cubic inverse close-packed arrangement of oxygen with Cu^{2+} and Fe^{3+} ions at two distinct crystallographic locations [25, 26]. CFNPs can be prepared by different preparation methods, including co-precipitation [27], hydrothermal process [28], sol-gel process [29], green method [30] and solid reaction process [31] were used to remove Pb^{2+} and Cd^{2+} ions from water. All the mentioned methods suffer from production of additional phases of Fe and Cu after preparation and the CFNPs purity was quite low [32]. Additionally, most of these techniques yield favorable outcomes in terms of achieving small particle size and controlling morphology. However, it is sometimes challenging to attain perfect control over the process, resulting in a poor production rate. In contrast, high-temperature solid-state processes are uncomplicated and readily scalable. Nevertheless, their ability to manipulate the characteristics of the end product is inadequate.

This study presents a novel advancement in the co-precipitation synthesis technique by implementing a copper ion substitution strategy within co-precipitated iron oxide nanoparticles (Fe_3O_4). The modified method facilitated the successful production of highly pure and single phase CFNPs. Utilizing these synthesized CFNPs, a comprehensive assessment was undertaken through batch equilibrium adsorption experiments aimed at efficiently removing Pb^{2+} and Cd^{2+} ions from wastewater. This experimental investigation meticulously explored essential parameters, including adsorption contact time, pH, adsorbent quantity, and initial metal ion concentrations, seeking to unravel the fundamental factors dictating the adsorption mechanisms.

Various isotherm and kinetic adsorption models were conducted, unveiling intricate insights into the adsorption kinetics and mechanisms driving this process. Moreover, an extensive investigation into the antibacterial efficacy of CFNPs against gram-positive and gram-negative pathogenic strains elucidates their multifaceted potential, emphasizing their significant role in environmental remediation strategies and various promising applications.

2. Experimental

2.1. Chemicals

All of the chemicals utilized in this work, including copper (II) nitrate trihydrate ($Cu(NO_3)_2.3H_2O$, 98%) purchased from Sigma-Aldrich, iron (III) chloride ($FeCl_3$, 98%) obtained from LOBA Chemie, ammonium ferrous sulphate hexahydrate (($NH_4)_2Fe(SO_4)_2.6H_2O$, 99%) sourced from MERCK Chemicals, Darmstadt, Germany. Nitrogen (N_2) gas. Sodium hydroxide (NaOH, 97%) and sodium borohydride ($NaBH_4$) were purchased from Thermo Fisher Scientific Inc., USA. All chemicals were used to prepare copper ferrite. All solutions and washings were performed using deionized water (Milli-Q Millipore, Billerica, MA, USA). The adsorption capacity of the synthesized material were investigated using two different types of heavy metals as adsorbates: lead nitrate ($Pb(NO_3)_2$, 99%) (LOBA Chemie, India). Cadmium sulphate ($CdSO_4$, 99%) from Sigma- Aldrich. Moller-Hinton agar is a bacteria nutrient, and dimethyl sulfoxide (1%DMSO) is a negative control. The collection of bacteria includes both gram-positive (S. pyrogenous and S.aureus) and gram-negative (E.Coli and P.aeruginosa) strains.

2.2. Preparation of Copper Ferrite Nanoparticles

The Modified co-precipitation approach was used to create CFNPs by substituting iron with copper. Fe_3O_4 nanoparticles were prepared by the traditional co-precipitation process [33, 34]. The preparation was started by adding 2.07 g of $FeCl_3$ and 2.5 g of ($NH_4)_2Fe(SO_4)_2.6H_2O$ to 400 mL of deionized water. The pH of the solution was then adjusted to 10 by adding NaOH solution in a drop wise slowly during stirring under N_2 flow. After stirring for several hours, the precipitate was washed several times with deionized water and left overnight at 60 ℃ for drying. 0.2 g of the resulting Fe_3O_4 powder was ultrasonicated in 200 mL of water for 10 min. For five minutes, 0.022 g of $NaBH_4$ and 0.02 g of $Cu(NO_3)_2.3H_2O$ each was ultrasonicated in 5 mL of water.

The three solutions were mixed and subjected to probe sonication for 30 min. Next, the mixture was shaken all night long. After repeatedly washing the precipitate in deionized water, it was left to dry overnight at 60 °C.

2.3. Instrumental

Raman spectrum (Bruker-Senterra,Germany) in the range from 100 to 3500 cm-1 using a 514.5 nm argon-ion laser. The crystal structure of the adsorbents was confirmed using an X-ray diffraction (XRD, X, Pert Pro – Panalytical, Netherland) diffractometer at room temperature with a Cu Kα radiation source (λ = 1.5404 Ao), power of 45 kV and 30 mA, 2 theta scans range from 4°-80°, step size of 0.02° and scan step time of 0.5 sec were used as the optimum condition in the measurements. The collected data were analyzed by X,Pert HighScore Plus software. The functionalized groups on the CFNPs were examined by Fourier transform infrared spectroscopy (FTIR, FT/IR-AT1 Mattson model Genesis Series, USA). The spectra of the samples were measured over the range 4000–400 cm−1 by mixing the sample powders with KBr at room temperature.

A high-resolution transmission electron microscope (HR-TEM, Tecnai G20, FEI, Netherland) was used to image the nanosorbent at 200 kV with a LaB6 electron source gun. Before the imaging, the sample was prepared by dispersing the powder in DI water, placing a few drops of the solution on carbon-coated copper grids and drying the grid at room temperature. The field emission-scanning electron microscope (FE-SEM) (FEI Quanta 250 FEG, USA) with an energy dispersion x-ray analysis (EDX) unit were used for characterization of particle size, the surface morphology and elemental composition of the prepared adsorbent, respectively.

To calculate the point of zero charge (PZC) of the sorbent, zeta-potential measurements (Zeta-sizer nano series, Nano ZS, Malvern Instruments, UK) was used, series of solutions were prepared with different pH values by suspension of the magnetic graphene nanocomposite at pH values from 3.0 to 9. The magnetic properties of the nanosorbent were measured using a vibrating sample magnetometer (VSM, Lakeshore 7410, USA) with an applied magnetic field of 20 KOe at room temperature.

The specific surface area and the pore size distributions curves by using the Barrett-Joyner-Hallenda (BJH) method of the prepared adsorbent were determined using nitrogen (adsorption/desorption) analyses at 77.35 K using a volumetric adsorption analyzer the Brunauer-Emmett-Teller (BET) (NOVA touch 4LX, Italy). Inductively coupled plasma mass spectrometry (ICP-MS, Agilent triple quad 8800, Germany) is used to determine the concentration of heavy metals present in wastewater (both before and after adsorption.

2.4. Adsorption experiments

CFNPs ability to adsorb Pb^{2+} and Cd^{2+} ions was investigated. Standard solutions were made from pure Pb $(NO_3)_2$ and cadmium sulphate ($CdSO_4$) at concentration 1000 mg/L. From this stock solution, lead (Pb^{2+}) and cadmium (Cd^{2+}) ions were produced at various concentrations ranging from 20 to 500 mg/L. The adsorption experiments were done at time range (20 - 200 minutes) and a pH range (from 2.0 to 8.0). Concentrations of Pb^{2+} and Cd^{2+} ions were measured by mass spectrophotometer (Agilent 8800 Triple Quad ICP-MS (8800), USA) after CFNPs were shaken with Pb^{2+} and Cd^{2+} ions at varied starting concentrations, ranging from 0.5 to 4.0 g/L.

To investigate the effects of CFNPs adsorption on the removal of Pb^{2+} and Cd^{2+} ions. Metal ions loading capacity q_e (mg/g) and removal efficiency (R%) were calculated using the following formulas:

$$\text{Removal \%} = \frac{C_i - C_f}{C_i} \times 100 \tag{1}$$

$$\text{Capacity } (q_e) = \frac{V(C_i - C_f)}{m} \tag{2}$$

Where (q_e) denotes the capacity for equilibrium adsorption, (C_i and C_f) denote the initial and final concentrations of metal ions (mg/L), v denotes the volume of the metal ion solution (L), and (m) is the mass of the adsorbent in grams.

2.5. Adsorption isotherm models

The adsorption mechanism of Pb^{2+} and Cd^{2+} ions over CFNPs was determined using isotherm calculations. Several different adsorption isotherm models can be used to test the adsorption process.

Several crucial models have been put through testing. At different equilibrium concentrations, the adsorption isotherms show how a solute that can be absorbed is spread between the liquid and solid phases. The type of surface phase, which can be thought of as a monolayer or multilayer, determines the analytical forms of adsorption isotherm equations. All of the adsorbed molecules in monolayer adsorption are in physical contact with the adsorbent's surface layer. In multilayer adsorption, more than one layer of molecules can fit into the adsorption region, and not every molecule that is adsorbed is in direct touch with the adsorbent's surface [35].

2.5.1. Langmuir adsorption isotherm model

Langmuir stated that the homogeneous surface of the adsorbent and monolayer-limitation of adsorption. The model may be stated mathematically as follows:

$$q_e = q_{max} - \left(\frac{1}{K_L}\right)\frac{q_e}{C_e} \tag{3}$$

Adsorption favorability between Pb^{2+} and Cd^{2+} ions and CFNPs, as measured by the Langmuir dimensionless constant separation factor (R_L), can be assumed with the following equation [36]:

$$R_L = \frac{1}{1 + C_e K_L} \tag{4}$$

Where C_e represents the concentration of Pb^{2+} and Cd^{2+} ions at equilibrium (mg/L), q_e represents the maximum amount of ions adsorbed at equilibrium (mg/g), and q_{max} represents the maximum theoretically adsorbed amount (mg/g). K_L represents the sorption equilibrium Langmuir constant (L/mg) [37].

2.5.2. Freundlich adsorption isotherm model

The two key concepts of Freundlich's model are the heterogeneity of the adsorbent's surface and the multilayer structure of the adsorption process [35]. The following mathematical formula can be used to express the model:

$$Ln\ q_e = Ln\ K_F + (1/n_F) \ln C_e \tag{5}$$

Where Ce is the equilibrium concentration of Pb^{2+} and Cd^{2+} ions in (mg/L), q_e is the highest quantity of Pb^{2+}, and Cd^{2+} ions adsorbed at equilibrium in (mg/g), n_F is the adsorption intensity or surface heterogeneity. K_F is the Freundlich constant or maximal adsorption capacity [37].

2.5.3. Adsorption isotherm model of Dubinin and Radushkevich (D-R)

Differentiating between physical and chemical adsorption is possible with the D-R isotherm model.

The linearized D-R isotherm model can be stated as follows [38, 39]:

$$Ln\ q_e = Ln\ q_m - \beta\ (\varepsilon^2) \tag{6}$$

The variable q_e represents the quantity of Pb^{2+} and Cd^{2+} ions that have been adsorbed at the state of equilibrium, expressed in units of (mol/g). The variable q_m represents the highest possible amount of adsorbate that can be adsorbed per unit mass of the adsorbent, measured in units of (mol/g). The constant β pertains to the adsorption energy and is expressed in units of (mol^2/kJ^2). ε (Polanyi potential) is $[RT \ln (1 + (1/C_e)]$; the symbol C_e represents the concentration at the equilibrium of Pb^{2+} and Cd^{2+} ions in units of (mol/L). R denotes the universal gas constant in units of (kJ/mol K), while T represents the temperature in units of (K).

2.6. Adsorption kinetics model

To show the rate of adsorption of Pb^{2+} and Cd^{2+} ions onto CFNPs. Two distinct kinetics models (pseudo-first order and pseudo-second order) were used to examine the experimental results.

2.6.1. Pseudo-first-order kinetic model

The process is more physisorption, as predicted by a pseudo-first-order kinetic model [40]. Following is an equation that represents the linearized pseudo-first-order kinetic model:

$$Ln\ (q_e - q_t) = Ln\ (q_e) - K_1 t \tag{7}$$

Where (q_e) is the amount of ions adsorbed in (mg/g) at equilibrium and (q_t) is the amount of ions adsorbed in (mg/g) at the time (t) (min), respectively, and (K_1) is the rate constant of adsorption (min^{-1}) [36].

2.6.2. Pseudo-second-order kinetic model

The pseudo-second-order kinetics model is commonly used to describe the rate-limiting stage of chemisorption [36]. The linear form of the pseudo-second-order kinetic model is represented by the following equation:

$$\frac{t}{qt} = \frac{1}{K_2 q_e^2} + \frac{t}{qe} \tag{8}$$

The following equation can be used to get the sorption rate (h) (mg/g min):

$$h = k_2 q_e^2 \tag{9}$$

Where (q_e and q_t) are the number of ions adsorbed in (mg/g) at equilibrium and the amount of ions adsorbed in (mg/g) at the time (*t*) (min), respectively, and (K_2) is the second order reaction rate constant of adsorption $(g.mg^{-1}. min^{-1})$ [17].

2.7. Antibacterial activity assay

The disc diffusion approach revealed that CFNPs had antibacterial effectiveness against gram-positive bacteria such as S. aureus and S. pyrogenous, as well as gram-negative bacteria such as E. Coli and P. aerogenous. The examination of the zone of inhibition was conducted using Moller-Hinton agar. Following the transfer of the bacteria from the pure culture to colonies that had comparable appearances, they were cultivated under aerobic conditions for 16 hours at a temperature of 37 °C, with the provision of nutrients. After the process of cleaning and sterilization, nutrient agar was introduced into Petri plates with a diameter of 25 mm. The bacterial culture was spread throughout the plates by using sterile cotton swabs and inoculating it onto Moller Hinton agar.

Four Petri dishes were utilized to cultivate distinct bacterial species on broth agar. Each dish contained two wells to exhibit the CFNPs (Cationic Fluorescent Nanoparticles) and the negative control, dimethyl sulfoxide (1%DMSO). 100 µL of the CFNPs solution extract with a concentration of 100 mg/mL was applied to the well of the testing dish. 100 µL of the 1% DMSO (negative controls) was applied to the matching well on the control plate. Ensuring the medication solution completely covered the whole surface of the well and reached its upper edges was crucial. The laminar flow hood is utilized to thoroughly desiccate the plates following approximately 30 minutes of exposure. The plates were inverted and incubated overnight until the cells had completely expanded. On the following day, a ruler assessed and quantified the area where bacterial proliferation was inhibited.

3. RESULTS AND DISCUSSION

3.1. Characterization of Prepared copper ferrite nanoparticles

3.1.1. Spectral analysis

Raman spectra are shown in Fig. **1 (A)** displaying six distinct bands at 216, 278, 394, 488, 590, and 1287 cm^{-1}. All of these spectra were identified as belonging to the cubic inverse-spinal structure of CFNPs [41]. While the bands at 278 and 394 cm^{-1} reflect the O-site mode, which corresponds to the local lattice effect in the octahedral sub-lattice, the band at 590 cm^{-1} reflects the T-site mode, which corresponds to the local lattice effect in the tetrahedral sub-lattice [28].

The intensity at 216 cm^{-1} may be due to CuO [42]. XRD patterns of CFNPs and magnetite are given in Fig. **1(B)**. Diffraction peaks for the cubic inverse phase of CFNPs nanoparticles are seen at 2θ = 30.30, 35.60, 43.30, 53.70, 57.10, 62.90, and 74.50, which correspond to the (2 2 0), (3 1 1), (4 0 0), (4 2 2), (5 1 1), (4 4 0), and (5 3 3) crystallographic planes of CFNPs (JCPDS file card number: 04-005-9479) [28]. At 2θ = 30.30, 35.60 and 62.90, three distinct signals for CFNPs have appeared. The XRD revealed the cubic inverse phase and high purity of the prepared CFNPs with no iron or copper impurities [32]. It is well known that magnetite and all spinel ferrites (MFe_2O_4, M: Zn, Mn, Cu,Co,..) have nearly the same XRD signal with the same peaks at the same 2θ positions as shown here in Fig.**1 (B)**. This was stated in many studies before [43–45].

The only way to differentiate between them is calculation of many parameters like crystallite size, FWHM and d-spacing. The crystallite size of the magnetite and CFNPs was calculated using Scherrer's formula and FWHM peak analysis [46]. The mean crystallite size of CFNPs and magnetite nanoparticles was 11.5 and 17 nm, respectively Table **1**, Table **2**. The lower intensity of CFNPs peak at (3 1 1) is a proof of lower crystallinity and lower crystallite size of CFNPs than that of magnetite [47]. d-spacing was calculated by Bragg's law using XRD results as shown in Table **1**,Table **2**. Additionally, peak FWHM values of CFNPs are less than Magnetite because of the higher crystallinity of magnetite [47].

It can be concluded from these results that d-spacing values for CFNPs are higher than that of magnetite which confirm the successful conversion of magnetite to CFNPs. From Table **1**, Table **2**, it is found that d-spacing increased after conversion of magnetite to CFNPs. This slight increase is due to atomic radius of Cu atom (0.127 nm) is higher than that of Iron (0.124 nm) with very little difference [48]. The CFNPs (FT-IR) spectrum is displayed in Fig. **1(C)**. The two absorption bands at 3420.4 cm^{-1} and 1619.8 cm^{-1} are due to H-O-H bending and stretching vibrational modes, respectively [49]. The (Cu-O) stretching vibration at tetrahedral sites and the (Fe-O) stretching vibration at octahedral sites account for the majority of the spectral absorptions in CFNPs. In octahedral sites, which are located at 542.9 cm^{-1} and 413 cm^{-1}, respectively [50].

3.1.2. Morphological characterizations

The surface morphology of CFNPs was characterized by FE-SEM in Fig. **2 (A)** using an, which reveals aggregated spherical particles with a random shape. The HR-TEM image in Fig. **2 (B, C)** further confirms the spherical morphology of the CF nanoparticles, with a mean size of 15 nm and 2.5 Ao d-spacing in agreement with XRD main peak at (3 1 1) plane [50]. The crystallographic planes of the CFNPs are (1 1 1), (2 2 0), (3 1 1), and (4 0 0), as shown in the selected area electron diffraction (SAED) pattern in Fig. **2 (D)** which match with XRD analysis. Additionally, the EDX spectrum of CFNPs displayed in Fig. **2 (E)** showed peaks of copper (Cu), iron (Fe), and oxygen (O) elements, confirming the chemical composition of CFNPs. The obtained spectrum not only confirmed the presence of a single phase but also emphasized the exceptional purity of the prepared material, as no other components were detected.

3.1.3. Physical properties characterization

To evaluate CFNPs viability as a dual-functional agent for heavy metal removal and antibacterial treatment in wastewater, their magnetic, surface area, and zeta potential properties were studied. The magnetic hysteresis loop of CFNPs is shown in Fig. **3(A)** using VSM. The CFNPs appear to have superparamagnetic activity because of their tiny particle size [51]. The net magnetization of the spinel lattice is primarily responsible for the soft ferrite's Ms value [52]. Ms of CFNPs measured by VSM was 52.68 emu/g at room temperature [53]. The high magnetization value proves the purity rather than the inverse cubic phase of CFNPs.

The nitrogen adsorption-desorption isotherms of CFNPs were studied using BET analysis at (77.35 K) and are depicted in Fig. **3 (B)**. As the International Union of Pure and Applied Chemistry (IUPAC) predicted, the N2 gas adsorption-desorption isotherm exhibits both the type IV curve and the H3 hysteresis loop. This activity demonstrates mesopore dominance. Hysteresis of type H3 denotes both the connectivity of pores and their random distribution. BET surface area measurement and t-plot analysis were carried out to determine the exact surface area of the produced material [7]. According to BET surface area measurement and t-plot analysis, the CFNPs had a pore width of 49 nm and a BET surface area of 85.027 m^2/g.

The zeta potential measurement of CFNPs shown in (Fig. **3 (C)**) is positive between 3.0 and 4.0. At pH = 4.0, CFNPs became negatively charged, as evidenced by a drop in zeta potential from 0 to -38 mV as pH was increased to 9.0. Aqua complexes (M-OH$_2^+$) are formed when the oxygen-containing groups on the surface of $CuFe_2O_4$ react with hydrogen ions. By ionizing oxygen-containing groups (-OH) into (-O-) groups, the surface of $CuFe_2O_4$ becomes negatively charged at higher pH values [54]. Because of their great magnetic susceptibility, CFNPs can be isolated using a powerful magnet. Magnetic separation is a significantly more efficient and time-saving solid-liquid separation method than centrifugal separation. The magnetic CFNPs could be separated from the water towards the strong magnet in less than 30 seconds. Removing the magnetic field allowed the CFNPs to be physically shaken into a uniform distribution once more once the field had been turned off.

3.2. Adsorption parameters study

3.2.1. Effect of pH

The adsorption process is significantly influenced by the pH of the solution as it affects the surface charge ionization and adsorbate speciation. With the initial metal ion concentration held constant at 20 mg/L, the effect of pH on the adsorption of Pb^{2+} and Cd^{2+} ions by CFNPs was investigated. The adsorption results are shown in (Figu. **4**), which demonstrates that at pHs of 8.0 and 7.0, respectively, CFNPs had the best removal effectiveness for the ions Pb^{2+} and Cd^{2+}. When the pH of the water is lowered, CFNPs are significantly less effective at removing Pb^{2+} and Cd^{2+} ions. Since positively charged metal ions compete with hydronium ions H_3O^+ for adsorption sites on the adsorbent surfaces, the removal effectiveness decreases at acidic pH levels [55]. Pb^{2+}, $Pb(OH)^+$, Cd^{2+}, and $Cd(OH)^+$ ions are all positively charged and readily attached to free binding sites on the surface of CFNPs at higher pH levels, leading to increased adsorption of Pb^{2+} and Cd^{2+} ions. Competition between H^+ ions disappears at these pH values [56].

3.2.2. Contact Time Effect

Fig. **5** shows how the amount of time in contact affects the amount of Pb^{2+} and Cd^{2+} ions absorbed by CFNPs. Due to their high surface area, CFNPs possess a high adsorption rate, which is demonstrated by the quick attainment of equilibrium adsorption in about 120 minutes.

Because of the high concentration of active sites and the specific surface area available for adsorbing Pb^{2+} and Cd^{2+} ions, CFNPs were able to maintain their adsorption capacity after 120 minutes, demonstrating their excellent adsorption efficiency. To ensure that adsorption equilibrium was achieved, subsequent experiments were conducted for 120 minutes. It was determined by adsorption studies that CFNPs have equilibrium adsorption capacities (qe) for Pb^{2+} and Cd^{2+} ions of (5.705 ± 0.285) and (3.715 ± 0.185), respectively.

3.2.3. Adsorbent dose effect

Examining the impact of the adsorbent dosage on the removal efficiency of CFNPs for Pb^{2+} and Cd^{2+} ions is crucial. This was investigated at varying adsorbent dosages, as shown in Fig. **6**. Increased CFNPs adsorbent doses resulted in greater removal efficiency for both metal ions. As the adsorbent's surface area grew, more active sites appeared on its surface, allowing for more efficient removal of metal ions. Saturation occurs because not all active sites are free for adsorption [57]. The maximum Pb^{2+} and Cd^{2+} ion removal efficiencies were (74.45 ± 3.722) % and (53.20 ± 2.660) %, respectively, at an adsorbent dosage of 4.0 g/L.

3.2.4. Effect of the initial concentrations of Pb^{2+} and Cd^{2+} ions

The sorption capacity of CFNPs for Pb^{2+} and Cd^{2+} ions has only been determined for a single initial concentration ranging from 20 to 1000 mg/L. Initial ion concentrations in wastewater may affect adsorption effectiveness. The adsorption of Pb^{2+} and Cd^{2+} ions by the CFNPs was also investigated. To study the effects of varying amounts of Pb^{2+} and Cd^{2+} ions, a series of solutions were prepared. The sorption capacity of CFNPs for Pb^{2+} and Cd^{2+} ions was greatly increased by the starting concentration of these ions, as shown in Fig. **7**.

As the initial concentrations of Pb^{2+} and Cd^{2+} ions were increased from 20 to 1000 mg/L, the adsorption capacity of CFNPs for Pb^{2+} ions increased from (3.02 ± 0.151) to (253.21 ± 12.660) mg/g, while for Cd^{2+} ions, it increased from (2.54 ± 0.127) to (250.56 ± 12.528) mg/g. The concentration at which Pb^{2+} and Cd^{2+} ions had the highest removal percent was 100 mg/L, while the concentration at which they had the lowest removal percent was 20 mg/L. However, after the concentration reaches 100 mg/L, the elimination begins to decrease as the concentration rises. The adsorption process for the Pb^{2+} and Cd^{2+} ions may be constrained in their ability to diffuse, contributing to this phenomenon.

Because there are fewer Pb^{2+} and Cd^{2+} ions than adsorption or ion exchange sites, the mass transfer barrier between the aqueous and solid phases lowers adsorption at low initial Pb^{2+} and Cd^{2+} ion concentrations. A major driving force for overcoming the pollutant's mass transfer resistances and boosting absorption was a higher starting concentration [58].

3.2.5. Adsorption Isotherm study

An adsorption isotherm is an important tool for characterizing the adsorption process under equilibrium conditions. The capacity of an adsorbent can be described using adsorption isotherms, which provides an understanding of the adsorption process. The linear equations of the Langmuir isotherm (Equations 3 and 4), the Freundlich isotherm (Equation 5), and the Dubinin-Radushkevich (D-R) isotherm (Equation 6) were used to evaluate the adsorption data obtained for the adsorption of Pb^{2+} and Cd^{2+} ions by the synthesized CFNPs. Using the Langmuir adsorption isotherm model, the Langmuir constant (KL) and the maximum capacity (qmax) were determined by analyzing the slope and intercept of the plot of (qe) (mg/g) vs. (qe/Ce), respectively [37].

The Freundlich constants (KF) and the surface heterogeneity (1/ nF) can be determined from the intercept and slope of the (ln qe) vs. (ln Ce) plot, respectively, when employing the Freundlich adsorption isotherm model [37]. The values of (qmax) and (β) were calculated using the D-R adsorption isotherm model. The intercept and slope of the (Ln qe) against (ε2) plots were used to calculate these values [38]. Adsorption isotherm data from various models, including Langmuir, Freundlich, and D-R, are shown in Fig. **8**. The determination of the validity of adsorption isotherm models was carried out through the calculation of the regression coefficient (R2).

The degree of success of the adsorption isotherm model in fitting the adsorption equilibrium data can be determined by the value of (R2), where a high value indicates a good fit and a low value indicates a weak fit [36]. Table **4** provides experimentally optimal values for the different adsorption kienetic parameters for Pb^{2+} and Cd^{2+} ions. The high value of the regression coefficient (R2) for the Freundlich and Dubinin-Radushkevich (D-R) models provides better match with CFNPs than the Langmuir model. Here, a complete explanation of the multilayer adsorption method on a heterogeneous adsorbent surface is provided.

In an ideal condition, the Freundlich adsorption isotherm would have a slope of ($1/nF$) between (0 and 1). As the value approaches zero, the surface of the adsorbent exhibits increased heterogeneity, resulting in a more nonlinear adsorption isotherm. When the value of ($1/nF$) exceeds (1), the adsorption isotherms indicate unfavourable heterogeneity [35]. In the case of CFNPs, $1/nF$ values for Pb^{2+} and Cd^{2+} ions were 1.0055 and 1.1358, respectively. These values proved that CFNPs are heterogeneous. The Langmuir dimensionless constant RL value is favourable when it falls within the range of (0 and 1). As it approaches (1), a linear adsorption isotherm is indicated. However, when (RL) is larger than (1), the adsorption isotherms are in an unfavourable state [36]. The adsorption of Pb^{2+} and Cd^{2+} ions onto CFNPs was favourable at all different initial concentrations, with (RL) values ranging from 0.025 to 0.814 (0<RL<1).This results indicate that

3.2.6. Adsorption Kinetics study

For better understanding of the adsorption mechanisms involved in the removal of Pb^{2+} and Cd^{2+} ions from wastewater by CFNPs, the kinetics of the process were investigated. The adsorption mechanism is influenced by both the chemical properties of the adsorbent and the mass transport method [38, 59]. Pseudo-first-order and pseudo-second-order kinetic models represented by (Equations 7, 8, and 9), were used to analyze the adsorption mechanisms and estimate the rate of mass transfer. At specified times, the adsorption capacity qt (mg/g) values were calculated. The experimental data was fitted to the pseudo-first-order and pseudo-second-order kinetic models to determine the adsorption rate. k1 and qe (mg/g) were obtained from the slope and intercept of the linearized plot, respectively.

The pseudo-first-order kinetics were calculated by plotting ln (qe-qt) vs. t (min) [60]. The pseudo-second-order kinetic model allowed us to determine the rate constant (K2) and activation energy (qe) from the slope and intercept, respectively, of a linear plot of (t/qt) versus t (min) [36]. The results of the pseudo-first-order and pseudo-second-order kinetic models are presented in Fig. **9**. The pseudo-first-order and pseudo-second-order rate constant values, correlation coefficient (R2) values, and qe values (experimental and estimated values) from Fig. **9** are all displayed in Table **3**.

However, the best-fit kinetics model for the removal of Pb^{2+} and Cd^{2+} ions from wastewater via CFNPs was determined by utilizing the discrepancies between experimental and estimated qe values and correlation coefficients (R2) values [36]. The R2 values for the pseudo-first-order kinetic model were much higher and far closer to unity than those for the pseudo second-order kinetic model, which has low R2 values. The theoretical qe values for removing Pb^{2+} and Cd^{2+} were also more in line with the experimental findings when using the pseudo-first-order kinetic model than when using the pseudo-second-order kinetic model.

Therefore, the adsorption process for removing Pb^{2+} and Cd^{2+} ions from wastewater using CFNPs was better defined by the pseudo-first-order kinetic model. So, the adsorption mechanism for Pb^{2+} and Cd^{2+} ions removal from wastewater by CFNPs was determined to be physisorption [40]. Based on the pseudo-first-order kinetic model, Pb2+ ions were quickly adsorbed to the surface of CFNPs because of high value of K1 for them in comparison with Cd^{2+} ions, and their capacity for equilibrium adsorption (qe) was higher than that of Cd^{2+} ions. When compared to other adsorbent materials shown in Table **5**, CFNPs were found to have better maximum adsorption capabilities for Pb^{2+} and Cd^{2+} ions, indicating their effectiveness in removing these toxic metals.

3.2.7. Antibacterial study

Many pathogenic bacteria are always present in waterbodies and cause waterborne disease. The bactericidal activity of CFNPs was studied against four bacteria (S.aureus, S. pyrogenous (gram-positive), E.Coli, and P.aeruginosa(gram-negative)). The disc diffusion method was used to examine the impact of CFNPs on these bacteria. Outcomes are presented in Fig. **10** describe the antibacterial activity of the CFNPs and the negative control (1%DMSO). Cellular proteins, mitochondria and DNA are destroyed because of the high rate of reactive oxygen (ROS) species generated from CFNPs. Additionally, by reducing the membrane's permeability, bacteria are killed by the combination of the negatively charged cell membrane and positively charged metal ions (copper and iron). Consequently, processed substances can be used to treat bacterial infections [61, 62]. Inhibition zone (mm) for S.aureus, S. pyrogenous, E.Coli, and P.aeruginosaon by different adsorbents are presented in Table **6**.

Table 1. CFNPs crystallite size according to XRD positions by Scherrer equation and d-spacing by Bragg's law

2θ	FWHM	Crystallite size (nm)	d-spacing
35	0.75	11.1	2.52201
43	0.73	12.14	2.09691
57	0.76	12.38	1.61038
62	0.92	10.7	1.47951

Table 2. Magnetite crystallite size according to XRD positions by Scherrer equation and d-spacing by Bragg's law

2θ	FWHM	Crystallite size (nm)	d-spacing
35	0.45	19.5	2.52009
43	0.59	14.9	2.08955
57	0.62	15.1	1.60854
62	0.52	18.8	1.47754

Table 3. Parameters describing the adsorption isotherms of CFNPs ability to remove Pb^{2+} and Cd^{2+} ions from wastewater

Metal ions	Langmuir adsorption isotherm model			Freundlich adsorption isotherm model			(D-R) adsorption isotherm model		
	q_{max} (mg/g)	K_L (L/mg)	R^2	$1/n_F$	K_F	R^2	q_{max} (mg/g)	β	R^2
Pb^{2+}	210.589	0.0163	0.0516	1.0055	0.6828	0.8520	131.388	0.0001318	0.9360
Cd^{2+}	149.996	0.0722	0.0018	1.1358	0.3102	0.8693	100.838	0.0001645	0.8475

Table 4 Adsorption kinetic parameters for Pb^{2+} and Cd^{2+} ion removal by CFNPs from wastewater

Metal ions	q_e (Experimental) (mg/g)	Pseudo-first-order kinetic model			Pseudo-second-order kinetic model			
		q_e (PFO) (mg/g)	K_1 (min^{-1})	R^2	q_e (PSO) (mg/g)	K_2 (g/mg min)	R^2	h (mg/g min)
Pb^{2+}	5.705	5.360	0.0169	0.723	21.88	0.000087	0.360	0.04193
Cd^{2+}	3.715	3.514	0.0101	0.763	-5.711	0.000418	0.135	0.01360

Table 5. Maximum adsorption capacity (q_{max}) for Pb^{2+} and Cd^{2+} ions by different adsorbents at room temperature is compared.

Metal ions	Adsorbents	Maximum adsorption capacity q_{max} (mg/g)	Reference
Pb^{2+}	1. CFNPs	17.8	[23]
	2. Modified activated carbon.	29.44	[63]
	3. CFNPs	31.1	[64]
	4. Carbon aerogel.	34.72	[65]
	5. Magnetic chitosan.	47.91	[66]
	6. $Cu_{0.5}Mg_{0.5}Fe_2O_4$	57.7	[64]
	7. Porous lignin xanthate resin	64.90	[67]
	8. Fe_3O_4	166.67	[68]
	9. Hydroxyapatite nanorods (nHAp)	192.30	[18]
	10. CFNPs	210.58	Present work
Cd^{2+}	1. CFNPs	17.54	[69]
	2. Activated carbon derived from bagasse	27.47–49.07	[70]
	3. Activated carbon derived from ceiba	19.59	[71]
	4. Polymer-modified Fe_3O_4 nanoparticles	29.60	[72]
	5. Magnetic graphene oxide	91.29	[73]
	6. Zinc ferrite ($ZnFe_2O_4$)	111.12	[74]
	7. nano crystallite hydroxyapatite	142.85	[75]
	8. CFNPs	149.99	Present work

Table 6. A comparison of the inhibition zone (mm) for S.aureus, S. pyrogenous, E.Coli, and P.aeruginosa by various adsorbents.

| Bacteria	Adsorbents	Concentration range	inhibition zone (mm)	Reference
S.aureus	1. GO-Ag	2 mg/mL	17 mm	[76]
	2. Mxene	5 µg	15 mm	[62]
	3. AgNPs	2 mg/ml	8 mm	[77]
	4. $CoFe_2O_4$	0.48 mg/mL	13 mm	[78]
	5. MgO-NPs	25 µg/mL	18.8 mm	[79]
	6. CFNPs	100 mg/mL	20 mm	Present work
S. pyrogenous	1. AgNPs	2 mg/mL	6 mm	[77]
	2. MgO-NPs	25 µg/mL	21 mm	[79]
	3. CFNPs	100 mg/mL	15 mm	Present work
E.Coli	1. GO-Ag	2 mg/mL	18 mm	[76]
	2. Mxene	5 µg	16 mm	[62]
	3. AgNPs	2 mg/ml	8 mm	[77]
	4. $CoFe_2O_4$	0.48 mg/mL	18 mm	[78]
	5. MgO-NPs	25 µg/mL	15 mm	[79]
	6. CFNPs	100 mg/mL	15 mm	Present work
P.aeruginosa	1. Mxene	5 µg	15 mm	[62]
	2. AgNPs	2 mg/mL	25 mm	[77]
	3. $CoFe_2O_4$	0.48 mg/mL	12 mm	[78]
	4. MgO-NPs	25 µg/mL	19 mm	[79]
	5. CFNPs	100 mg/mL	10 mm	Present work
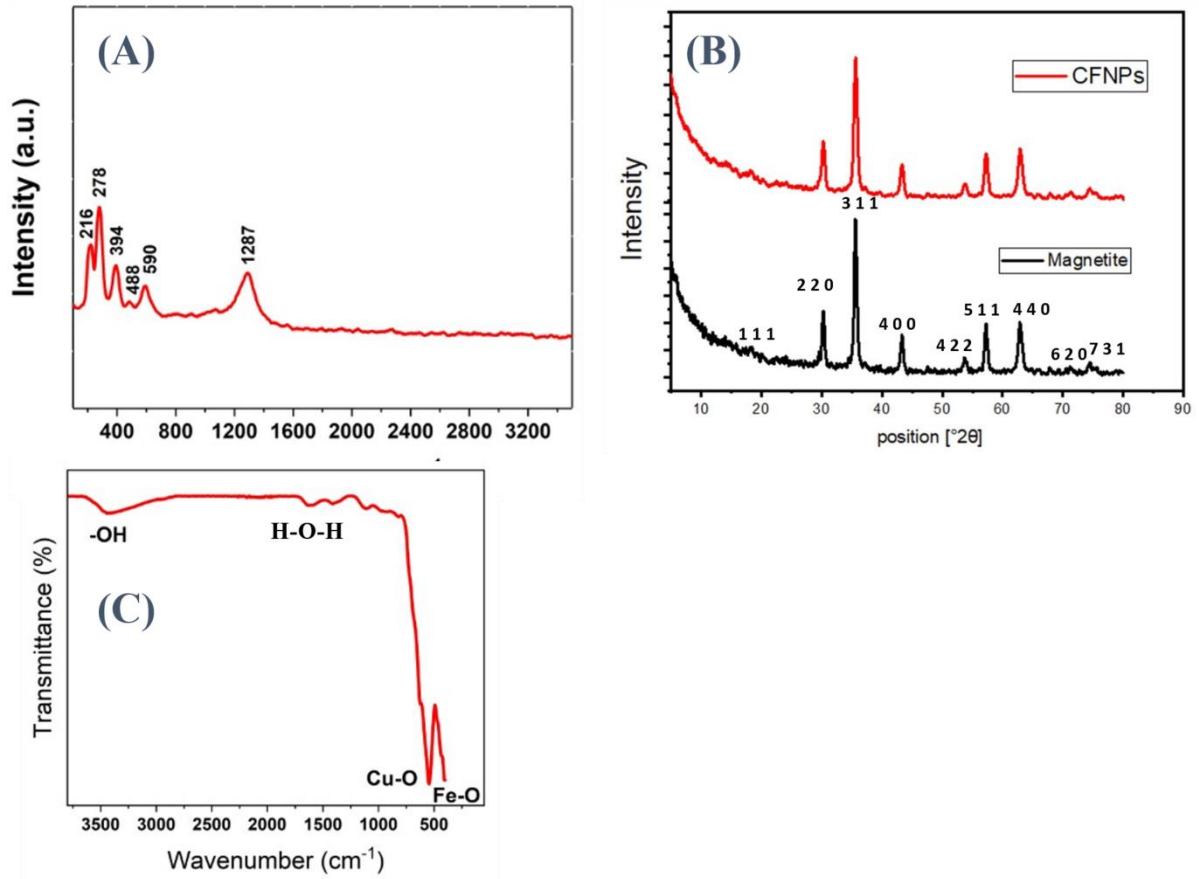
Fig. 1 (A) Raman spectrum and **(B)** XRD patterns of CFNPs and magnetite, **(C)** FTIR spectrum of CFNPs.
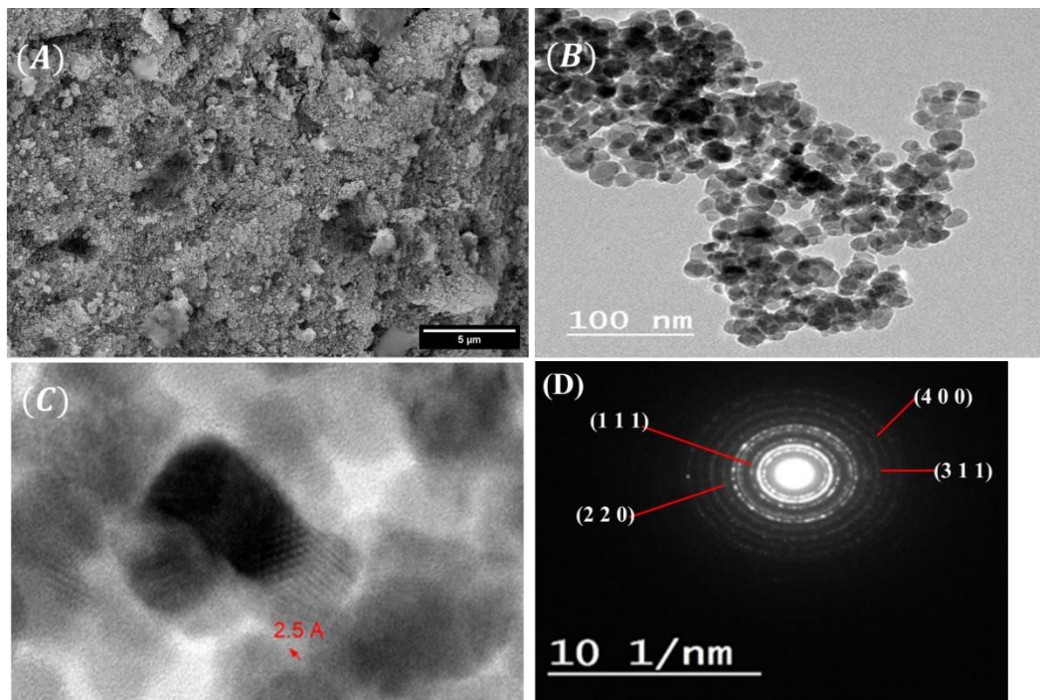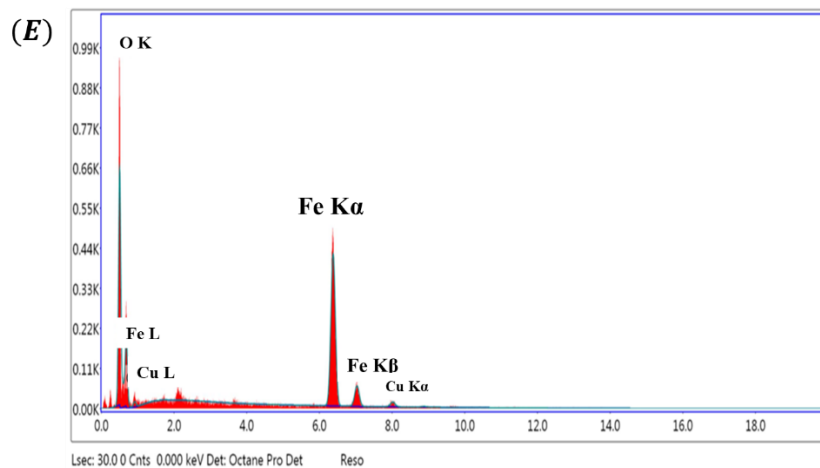
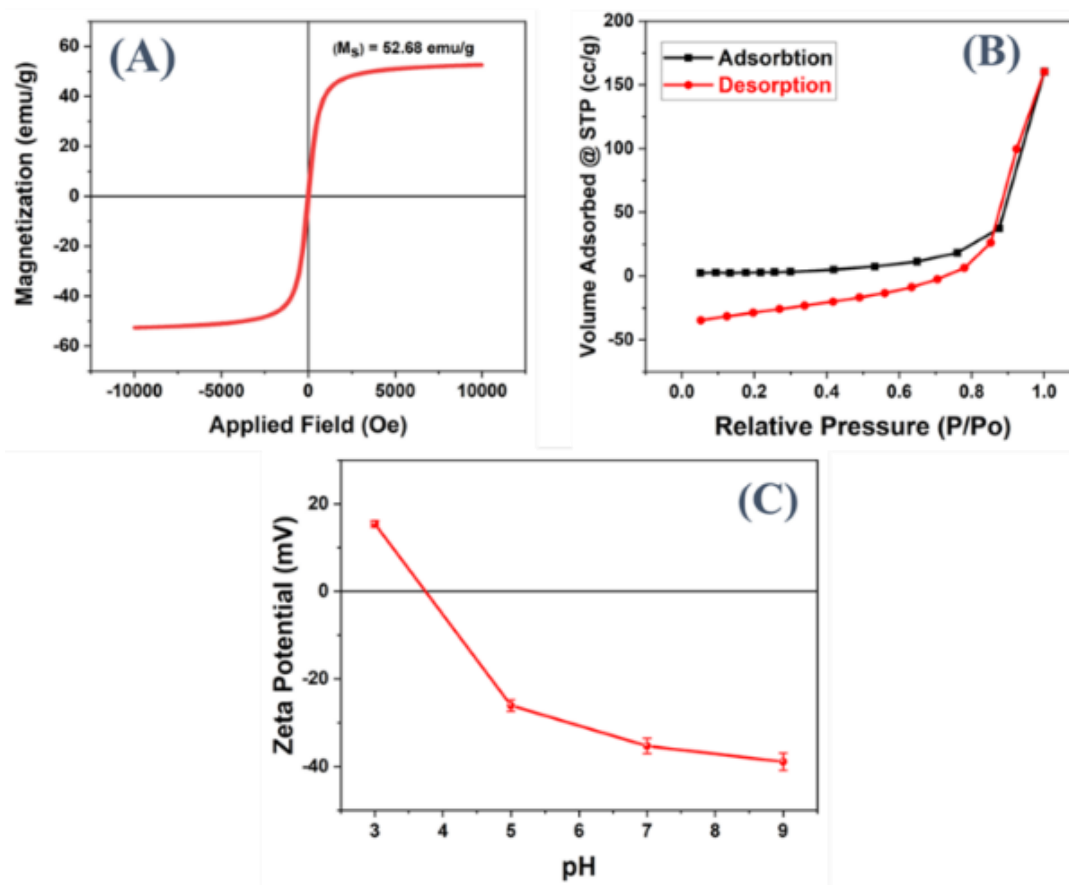**Fig. 2 (A)** FE-SEM, **(B, C)** HR-TEM, **(D)** SAED patterns and **(E)** EDX spectrum of CFNPs.

Fig. 3 (A) Magnetic Hysteresis (M-H) loops, **(B)** Nitrogen adsorption/desorption isotherms, and **(C)** Chart of zeta potential versus pH of CFNPs.
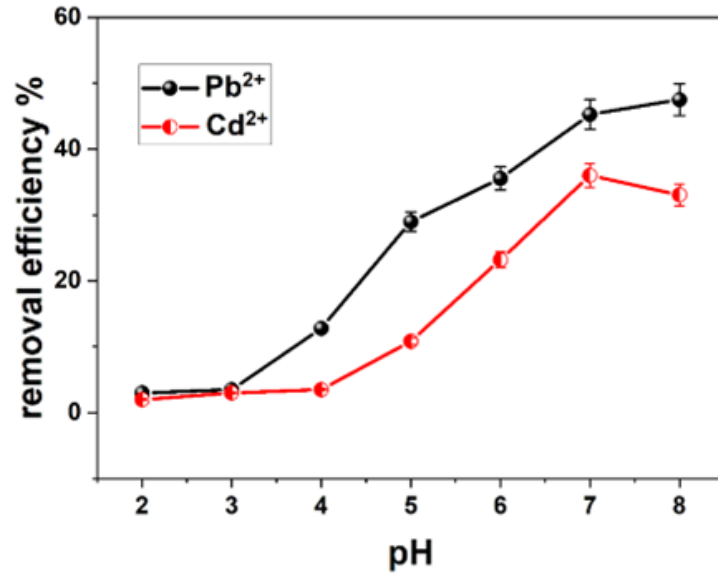
Fig. 4 Analysis of an effect of pH on the removal efficiency of 20 mg/L Pb^{2+} and Cd^{2+} ions onto CFNPs at 25 °C and 120 min using a dosage of 2 g/L of adsorbent.
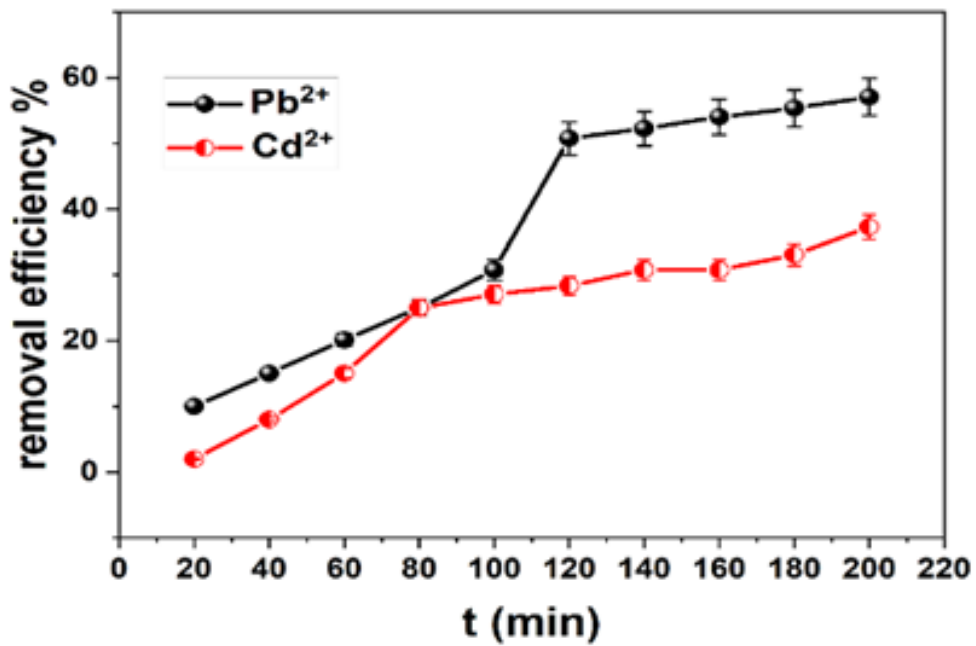
Fig. 5 Contact time affected the removal efficiency of Pb2+ and Cd^{2+} ions (20 mg/L) onto CFNPs at 2 g/L, 25 °C and pH 5.0.
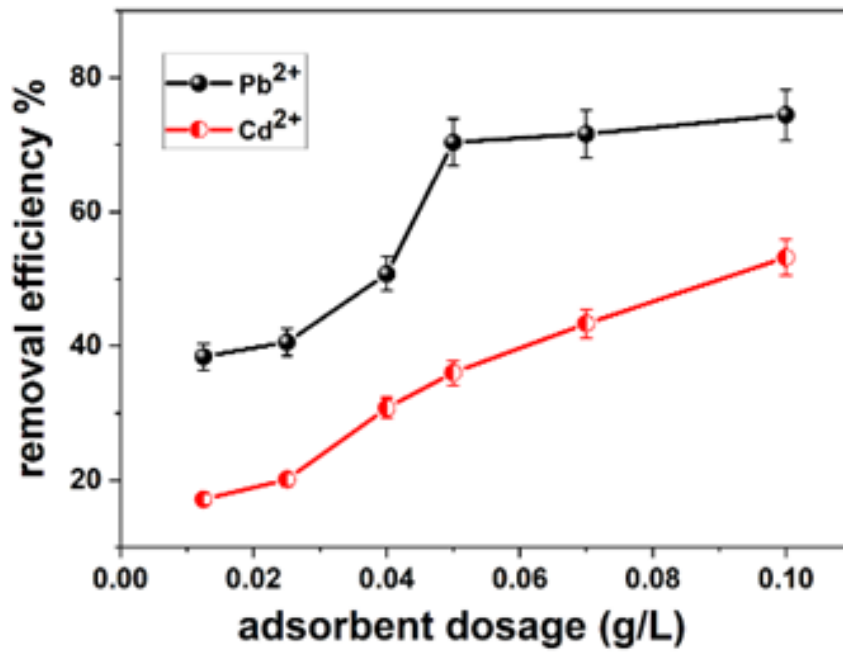
Fig. 6 The removal efficiency of Pb^{2+} and Cd^{2+} ions onto CFNPs was shown to be affected by the adsorbent dosage, initial concentration 20 mg/L, time 120 min, temperature 25 °C, and pH 5.0.
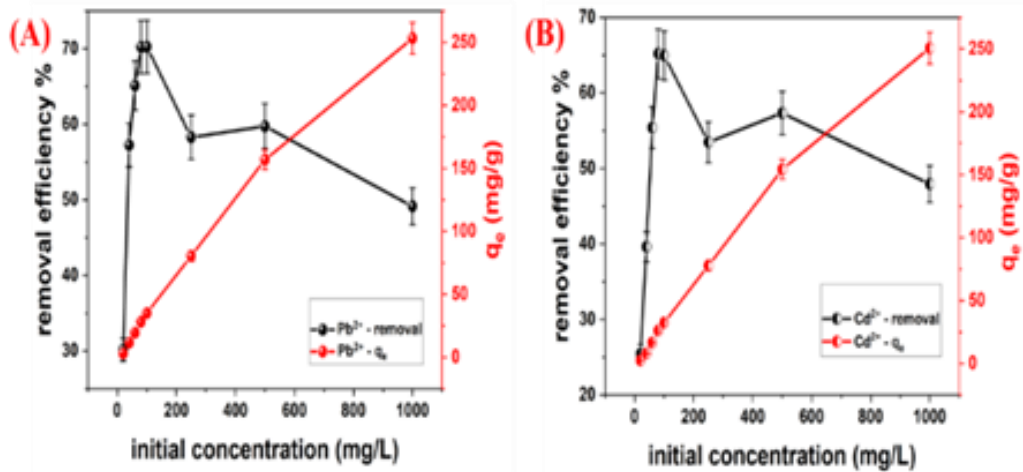

Fig. 7 Removal efficiency and adsorption capacity of (A) Pb^{2+} and (B) Cd^{2+} ions onto CFNPs as a function of ion concentration at 2 g/L adsorbent dose, 120 min contact time, 25 °C temperature, and pH 5.0.
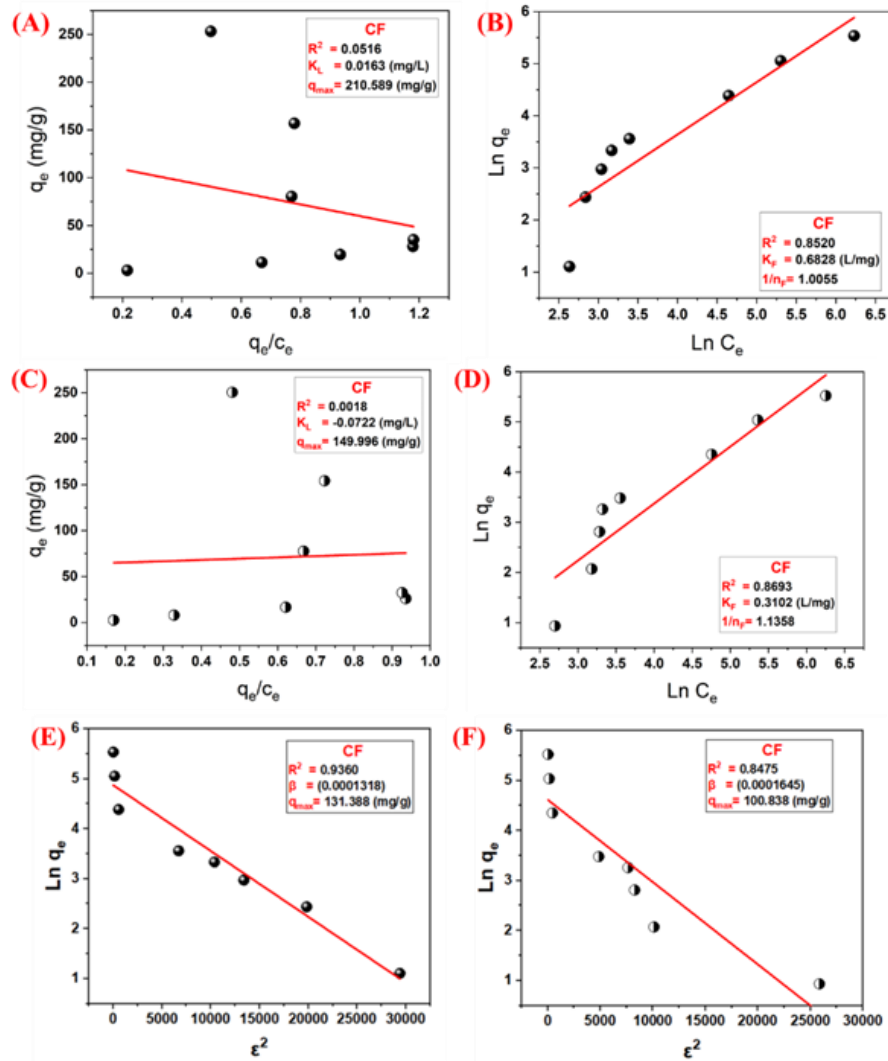
57

Fig. 8 Adsorption isotherms of **Pb^{2+}** and **Cd^{2+}** removal from wastewater by using CFNPs have been studied. **(A)** and **(C)** depict the Langmuir model for **Pb^{2+}** and **Cd^{2+}**, respectively. The Freundlich model for **Pb^{2+}** and **Cd^{2+}** ions are depicted in **(B)** and **(D)**, respectively. **(E)** and **(F)** depict the Dubinin-Radushkevich (D-R) model for **Pb^{2+}** and **Cd^{2+}**, respectively.
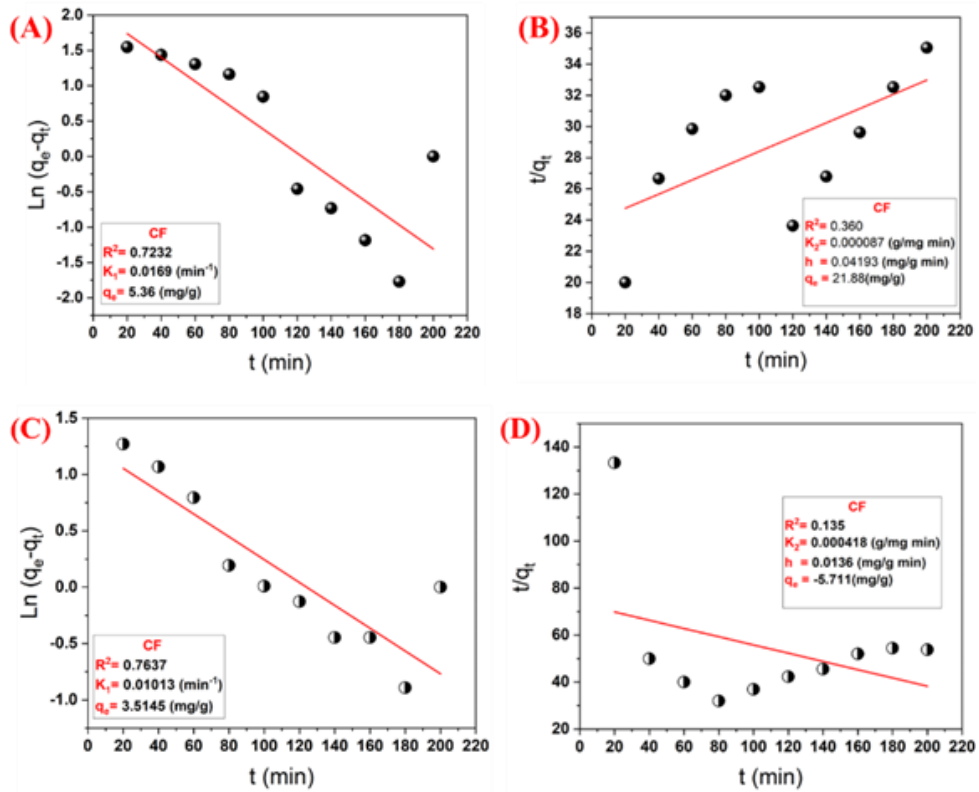
Fig. 9 Adsorption kinetics studies of Pb^{2+} and Cd^{2+} removal from wastewater utilizing CFNPs. **(A)** and **(C)** depict pseudo-first-order models of Pb^{2+} and Cd^{2+}, respectively. The Pseudo-second-order Pb^{2+} and Cd^{2+} ions are represented in **(B)** and **(D)**, respectively.
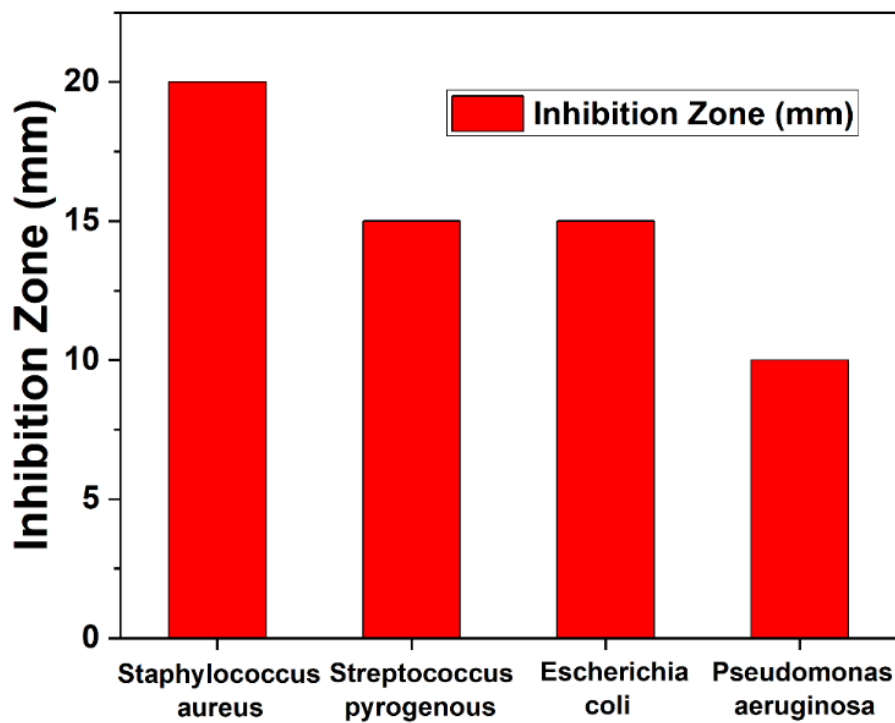

Fig. 10 The antibacterial activity of the CFNPs against four bacteria (S.aureus, S. pyrogenous, E.Coli, and P.aeruginosa).

4. Conclusion

CFNPs were manufactured using a unique method (Modified co-precipitation). This strategy is simple, cheap, and safe. The findings indicated that CFNPs were synthesised with an average diameter of 15 nm in an irregular form. Under different pH levels, contact times, initial Pb^{2+} and Cd^{2+} ions concentrations, and adsorbent dosage, CFNPs were tested for usage in aqueous Pb^{2+} and Cd^{2+} ions adsorption from wastewater. The pseudo-first-order and Dubinin-Radushkevich (D-R) models provide a good fit for the adsorption kinetics and the adsorption isotherm, respectively. In addition, antibacterial activity was evaluated to ensure the CFNPs would be effective against bacteria and metal ions. When tested against S. aureus, S. pyrogenous, E. coli, and P. aeruginosa, the inhibition zones for CFNPs at a concentration of 100 mg/mL were found to be 20, 15, 15, and 10 mm, respectively. To the best of our knowledge, heavy metal ion uptake and antibacterial activity in CFNPs have been observed. As a result, two types of water pollution can be managed simultaneously: one caused by heavy metals, the other by bacteria.

5. References

1. **S., Bhattacharya., A. B., Gupta., A., Gupta., and A., Pandey. (2018).** Introduction to Water Remediation: Importance and Methods, Energy, Environ. Sustain., **pp. 3–8, doi: 10.1007/978-981-10-7551-3_1.**

2. **A., Ahmad. and R., Ghufran. (2018).** Review on industrial wastewater energy sources and carbon emission reduction : towards a clean production, Int. J. Sustain. Eng., **vol. 7038, pp. 1–11, doi: 10.1080/19397038.2018.1423647.**

3. **R. K., Gautam., S. K., Sharma., S., Mahiya., and M. C., Chattopadhyaya. (2014).** CHAPTER 1. Contamination of Heavy Metals in Aquatic Media: Transport, Toxicity and Technologies for Remediation, Heavy Met. Water, no. August, **pp. 1–24, doi: 10.1039/9781782620174-00001.**

4. **S. Engineering, T. H. Kong, H. Hom, and H. Kong. (2006).** Journal of Environmental Science and Health, Part A : Toxic / Hazardous Substances and Environmental Engineering Vegetation Composition and Heavy Metal Uptake by Wild Plants at Three Contaminated Sites in Xiangxi Area, no. September 2014, **pp. 37–41, doi: 10.1080/10934520500298838.**

5. **E., Pehlivan., B. H., Yanik., G., Ahmetli., and M., Pehlivan. (2008).** Equilibrium isotherm studies for the uptake of cadmium and lead ions onto sugar beet pulp, Bioresour. Technol., **vol. 99, no. 9, pp. 3520–3527, doi: 10.1016/j.biortech.2007.07.052.**

6. **F., Edition., I., The., and F., Addendum.,** No Title.

7. **S., Chella., & et al. (2015).** Solvothermal synthesis of $MnFe_2O_4$ -graphene composite-Investigation of its adsorption and antimicrobial properties, Appl. Surf. Sci., **vol. 327, pp. 27–36, doi: 10.1016/j.apsusc.2014.11.096.**

8. **CDC. (2019).** Antibiotic Resistance Threats in The United States, Cdc, **vol. 10, no. 1, 2019, doi: 10.1186/s13756-020-00872-w.**

9. **E. S., Agudosi., & et al. (2018).** Journal of Environmental Chemical Engineering Pilot study of in-line continuous flocculation water treatment plant, J. Environ. Chem. Eng., **vol. 6, no. 6, pp. 7185–7191, doi: 10.1016/j.jece.2018.11.001.**

10. **S., Rahimi., & et al. (2014).** Photocatalytic removal of cadmium (II) and lead (II) from simulated wastewater at continuous and batch system, **vol. 3, no. 2, pp. 90–94, doi: 10.4103/2277-9183.139756.**

11. **I. J. M., Process., T., Motsi., N. A., Rowson., and M. J. H., Simmons. (2009).** Adsorption of heavy metals from acid mine drainage by natural zeolite," Int. J. Miner. Process., **vol. 92, no. 1–2, pp. 42–48, doi: 10.1016/j.minpro.2009.02.005.**

12. **V., Srivastava., C. H., Weng., V. K., Singh., and Y. C., Sharma. (2011).** Adsorption of Nickel Ions from Aqueous Solutions by Nano Alumina : Kinetic, Mass Transfer, and Equilibrium Studies, **pp. 1414–1422.**

13. **W., Chooaksorn. (2016).** NANOSORPTION - MEMBRANE FILTRATION FOR HEAVY METAL REMOVAL BY NANOSORPTION - MEMBRANE FILTRATION FOR HEAVY METAL REMOVAL.

14. **L. K., Wang., D. A., Vaccari., Y., Li., and N. K., Shammas.** Chemical Precipitation, **vol. 3.**

15. **Y., Song., S., Lei., J., Zhou., and Y., Tian. (2015).** Removal of heavy metals and cyanide from gold mine waste-water by adsorption and electric adsorption, **no. July, doi: 10.1002/jctb.4859.**

16. **M., Adel., M. A., Ahmed., M. A., Elabiad., and A. A., Mohamed. (2022).** Removal of heavy metals and dyes from wastewater using graphene oxide-based nanomaterials: A critical review, Environ. Nanotechnology, Monit. Manag., **vol. 18, no. June, p. 100719, doi: 10.1016/j.enmm.2022.100719**.

17. **T. A., Salah., A. M., Mohammad., M. A., Hassan., and B. E., El-Anadouli. (2014).** Development of nano-hydroxyapatite/chitosan composite for cadmium ions removal in wastewater treatment, J. Taiwan Inst. Chem. Eng., **vol. 45, no. 4, pp. 1571–1577, doi: 10.1016/j.jtice.2013.10.008.**

18. **A. M., Mohammad., T. A., Salah Eldin., M. A., Hassan., and B. E., El-Anadouli. (2017).** Efficient treatment of lead-containing wastewater by hydroxyapatite/chitosan nanostructures, Arab. J. Chem., **vol. 10, no. 5, pp. 683–690, doi: 10.1016/j.arabjc.2014.12.016.**

19. **S., Kamel., A. A., El-Gendy., M. A., Hassan., M., El-Sakhawy., and I., Kelnar. (2020).** Carboxymethyl cellulose-hydrogel embedded with modified magnetite nanoparticles and porous carbon: Effective environmental adsorbent, Carbohydr. Polym., **vol. 242, no. April, doi: 10.1016/j.carbpol.2020.116402.**

20. **N. N., Nassar., (2010). Rapid removal and recovery of Pb (II)** from wastewater by magnetic nanoadsorbents, J. Hazard. Mater., **vol. 184, no. 1–3, pp. 538–546, doi: 10.1016/j.jhazmat.2010.08.069**.

21. **E., Kim., C., Lee., Y., Chang., and Y., Chang. (2013).** Hierarchically Structured Manganese Oxide-Coated Magnetic Nanocomposites for Efficient Removal of Heavy Metal Ions from Aqueous Systems, **doi: 10.1021/am402615m.**

22. **M. K., Abbas., & et al.** Magnetic Ferrites-Based Hybrids Structures for the Heavy Metal Removal. Springer International Publishing. **doi: 10.1007/978-3-030-79960-1_12.**

23. **Y. J., Tu., C. F., You., M. H., Chen., and Y. P., Duan. (2017).** Efficient removal/recovery of Pb onto environmentally friendly fabricated copper ferrite nanoparticles, J. Taiwan Inst. Chem. Eng., **vol. 71, pp. 197–205, doi: 10.1016/j.jtice.2016.12.006.**

24. **M. K., Bharti., S., Gupta., S., Chalia., I., Garg., P., Thakur., and A., Thakur. (2020).** Potential of Magnetic Nanoferrites in Removal of Heavy Metals from Contaminated Water : Mini Review, **pp. 3651–3665.**

25. **S. K., Ka., P., Novak., and E. E. P., Wohlfarth. (1982).** chapter 4 OXIDE SPINELS *, **vol. 2.**

26. **Y. M. Z. Ã., Ahmed., M. M., Hessien., M. M., Rashad., and I. A., Ibrahim. (2009).** Journal of Magnetism and Magnetic Materials Nano-crystalline copper ferrites from secondary iron oxide (mill scale), **vol. 321, pp. 181–187, doi: 10.1016/j.jmmm.2008.08.100.**

27. **N. M., Mahmoodi., (2011).** Photocatalytic ozonation of dyes using copper ferrite nanoparticle prepared by co-precipitation method, Desalination, **vol. 279, no. 1–3, pp. 332–337, doi: 10.1016/j.desal.2011.06.027.**

28. **L. K., Wu, & et al. (2017).** Highly porous copper ferrite foam: A promising adsorbent for efficient removal of As(III) and As(V) from water, J. Hazard. Mater., **vol. 347, pp. 15–24, 2018, doi: 10.1016/j.jhazmat. 12.048.**

29. **S. S., Tha., and H., Htoo. (2020).** PREPARATION AND STRUCTURAL PROPERTIES OF COPPER FERRITE BY SOL-GEL METHOD, **vol. XVIII, no. 2.**

30. **G., Sreekala., A., Fathima Beevi., R., Resmi., and B., Beena. (2019).** Removal of lead (II) ions from water using copper ferrite nanoparticles synthesized by green method, Mater. Today Proc., **vol. 45, no. xxxx, pp. 3986–3990, doi: 10.1016/j.matpr.2020.09.087.**

31. **Z., Ye., Z., Deng., L., Zhang., J., Chen., G., Wang., and Z., Wu. (2020).** The structure of copper ferrite prepared by five methods and its catalytic activity on lignin oxidative degradation," Mater. Res. Express, **vol. 7, no. 3, p. 35007, , doi: 10.1088/2053-1591/ab778b.**

32. **R. S., Yadav., & et al. (2017).** Structural, dielectric, electrical and magnetic properties of $CuFe_2O_4$ nanoparticles synthesized by honey mediated sol–gel combustion method and annealing effect," J. Mater. Sci. Mater. Electron., **vol. 28, no. 8, pp. 6245–6261, doi: 10.1007/s10854-016-6305-4.**

33. **F., Mérida., & et al. (2015).** Optimization of synthesis and peptization steps to obtain iron oxide nanoparticles with high energy dissipation rates, J. Magn. Magn. Mater., **vol. 394, pp. 361–371, doi: 10.1016/j.jmmm.2015.06.076.**

34. **S., Savliwala., & et al. (2019).** Magnetic nanoparticles. Elsevier Inc., **doi: 10.1016/B978-0-12-816662-8.00013-8.**

35. **R., Saadi., Z., Saadi., R., Fazaeli., and N. E., Fard. (2015).** Monolayer and multilayer adsorption isotherm models for sorption from aqueous media Monolayer and multilayer adsorption isotherm models for sorption, **no. May, doi: 10.1007/s11814-015-0053-7.**

36. **N., Ueda Yamaguchi., R., Bergamasco., and S., Hamoudi., (2016).** Magnetic $MnFe_2O_4$-graphene hybrid composite for efficient removal of glyphosate from water, Chem. Eng. J., **vol. 295, pp. 391–402, doi: 10.1016/j.cej.2016.03.051.**

37. **P., Palanivell., O. H., Ahmed., O., Latifah., N., Muhamad., and A., Majid.** applied sciences Adsorption and Desorption of Nitrogen , Phosphorus , Potassium , and Soil Buffering Capacity Following Application of Chicken Litter Biochar to an Acid Soil, **pp. 1–18.**

38. **J., Lin., Y., Zhan., and Z., Zhu. (2011).** Colloids and Surfaces A : Physicochemical and Engineering Aspects Adsorption characteristics of copper (II) ions from aqueous solution onto humic acid-immobilized surfactant-modified zeolite," Colloids Surfaces A Physicochem. Eng. Asp., **vol. 384, no. 1–3, pp. 9–16, doi: 10.1016/j.colsurfa.2011.02.044.**

39. **N. B., Singh., and K., Rachna. (2020).** Copper ferrite-Polyaniline nanocomposite and its application for Cr (VI) ion removal from aqueous solution, Environ. Nanotechnology, Monit. Manag., **vol. 14, no. August 2019, p. 100301, doi: 10.1016/j.enmm.2020.100301.**

40. **I., Othman., M., Abu Haija., P., Kannan., and F., Banat. (2020).** Adsorptive Removal of Methylene Blue from Water Using High-Performance Alginate-Based Beads," Water. Air. Soil Pollut., **vol. 231, no. 8, doi: 10.1007/s11270-020-04751-3.**

41. **B., Mondal., & et al. (2019).** Sonochemically Synthesized Spin-Canted $CuFe_2O_4$ Nanoparticles for Heterogeneous Green Catalytic Click Chemistry, ACS Omega, **vol. 4, no. 9, pp. 13845–13852, doi: 10.1021/acsomega.9b01477.**

42. **L. K., Wu., et al. (2018).** Graphene oxide/CuFe2O4 foam as an efficient absorbent for arsenic removal from water, Chem. Eng. J., **vol. 334, no. November 2017, pp. 1808–1819, doi: 10.1016/j.cej.2017.11.096.**

43. **A., Antonello., & et al. (2017).** Synergy of Miniemulsion and Solvothermal Conditions for the Low-Temperature Crystallization of Magnetic Nanostructured Transition-Metal Ferrites, Chem. Mater., **vol. 29, no. 3, pp. 985–997, Feb., doi: 10.1021/acs.chemmater.6b03467.**

44. **E., Solano., C., Frontera., T., Puig., X., Obradors., S., Ricart., and J., Ros. (2014).** Neutron and X-ray diffraction study of ferrite nanocrystals obtained by microwave-assisted growth. A structural comparison with the thermal synthetic route, in Journal of Applied Crystallography, **vol. 47, no. 1, pp. 414–420. doi: 10.1107/S1600576713032895.**

45. **M., Sorescu., A., Grabias., and L., Diamandescu. (2001).** From Magnetite to Cobalt Ferrite," J. Mater. Synth. Process., **vol. 9, no. 3, pp. 119–123, doi: https://doi.org/10.1023/A:1013241312932.**

46. **A., Monshi., M. R., Foroughi., and M. R., Monshi. (2012).** Modified Scherrer Equation to Estimate More Accurately Nano-Crystallite Size Using XRD, World J. Nano Sci. Eng., **vol. 02, no. 03, pp. 154–160, doi: 10.4236/wjnse.2012.23020.**

47. **R. M., Ali., M. R., Elkatory., and H. A., Hamad. (2020).** Highly active and stable magnetically recyclable $CuFe_2O_4$ as a heterogenous catalyst for efficient conversion of waste frying oil to biodiesel," Fuel, **vol. 268, no. January, p. 117297, May, doi: 10.1016/j.fuel.2020.117297.**

48. **William D., Callister., and David G., Rethwisch. (2015).** Fundamentals of Materials Science and Engineering: An Integrated Approach (Fifth Edition), Wiley, **p. 964.**

49. **X., Zhang., and S. P., Sander. (2011).** Infrared absorption spectra of the CO 2/H 2O complex in a cryogenic nitrogen matrix-detection of a new bending frequency, J. Phys. Chem. A, **vol. 115, no. 35, pp. 9854–9860, doi: 10.1021/jp203739v.**

50. G., Sreekala., A., Fathima Beevi., R., Resmi., and B., Beena. (2019). Removal of lead (II) ions from water using copper ferrite nanoparticles synthesized by green method, Mater. Today Proc., **vol. 45, no. xxxx, pp. 3986–3990, doi: 10.1016/j.matpr.2020.09.087.**

51. W., Wang., K., Cai., X., Wu., X., Shao., and X., Yang. (2017). A novel poly (m-phenylenediamine)/reduced graphene oxide/nickel ferrite magnetic adsorbent with excellent removal ability of dyes and Cr(VI), J. Alloys Compd., **vol. 722, no. Vi, pp. 532–543, doi: 10.1016/j.jallcom.2017.06.069.**

52. F. H., Mulud., N. A., Dahham., and I. F., Waheed. (2020). Synthesis and Characterization of Copper Ferrite Nanoparticles, IOP Conf. Ser. Mater. Sci. Eng., **vol. 928, no. 7, doi: 10.1088/1757-899X/928/7/072125.**

53. M. M., Rashad., R. M., Mohamed., M. A., Ibrahim., L. F. M., Ismail., and E. A., Abdel-Aal. (2012). Magnetic and catalytic properties of cubic copper ferrite nanopowders synthesized from secondary resources, Adv. Powder Technol., **vol. 23, no. 3, pp. 315–323, doi: 10.1016/j.apt.2011.04.005.**

54. A. H., Kamel, A. A., Hassan., A. E. E., Amr., and H. H., El-shalakany. Synthesis and Characterization of $CuFe_2O_4$ Nanoparticles Modified with Polythiophene : Applications to Mercuric Ions Removal.

55. C., Namasivayam., and K., Ranganathan. (1995). Removal of pb(ii), cd(ii), ni(ii) and mixture of metal ions by adsorption onto 'waste' fe(iii)/cr(iu) hydroxide and fixed bed studies, Environ. Technol. (United Kingdom), **vol. 16, no. 9, pp. 851–860, doi: 10.1080/09593330.1995.9618282.**

56. V. C., Srivastava., I. D., Mall., and I. M., Mishra. (2006). Equilibrium modelling of single and binary adsorption of cadmium and nickel onto bagasse fly ash, Chem. Eng. J., **vol. 117, no. 1, pp. 79–91, doi: 10.1016/j.cej.2005.11.021.**

57. K. G., Bhattacharyya., and S., Sen Gupta. (2007). Adsorptive accumulation of Cd(II), Co(II), Cu(II), Pb(II), and Ni(II) from water on montmorillonite: Influence of acid activation, J. Colloid Interface Sci., **vol. 310, no. 2, pp. 411–424, doi: 10.1016/j.jcis.2007.01.080.**

58. S., Tezer. (2005). Biosorption of reactive dyes on the green alga Chlorella vulgaris, **vol. 40, pp. 1347–1361, doi: 10.1016/j.procbio.2004.06.007.**

59. M., Achak., A., Hafidi., N., Ouazzani., S., Sayadi., and L., Mandi. (2009). Low cost biosorbent ' banana peel ' for the removal of phenolic compounds from olive mill wastewater : Kinetic and equilibrium studies, **vol. 166, pp. 117–125, doi: 10.1016/j.jhazmat.2008.11.036.**

60. G., Abimbola., Z., Zaman., and P., Adeniyi. (2017). Equilibrium, kinetic, and thermodynamic studies of lead ion and zinc ion adsorption from aqueous solution onto activated carbon prepared from palm oil mill ef fl uent, J. Clean. Prod., **vol. 148, pp. 958–968, doi: 10.1016/j.jclepro.2017.02.047.**

61. A., Abass., A., Khan., S., Dwivedi., J., Musarrat., and A., Azam. (2018). Antibacterial and Antibiofilm Activity of Barium Titanate Nanoparticles," Mater. Lett., **vol. 229, pp. 130–133, doi: 10.1016/j.matlet.2018.06.107.**

62. I. A., Alsafari., S., Munir., S., Zulfiqar., M. S., Saif., M. F., Warsi., and M., Shahid. (2021). Synthesis, characterization, photocatalytic and antibacterial properties of copper Ferrite/MXene ($CuFe_2O_4/Ti_3C_2$) nanohybrids, Ceram. Int., **vol. 47, no. 20, pp. 28874–28883, , doi: 10.1016/j.ceramint.2021.07.048.**

63. J., Goel., K., Kadirvelu., C., Rajagopal., and V., Kumar. (2005). Removal of lead (II) by adsorption using treated granular activated carbon : Batch and column studies, **vol. 125, pp. 211–220, doi: 10.1016/j.jhazmat.2005.05.032.**

64. C., Van Tran., D. V., Quang., H. P., Nguyen Thi., T. N., Truong., and D. D., La. (2020). Effective Removal of Pb(II) from Aqueous Media by a New Design of Cu-Mg Binary Ferrite, ACS Omega, **vol. 5, no. 13, pp. 7298–7306, doi: 10.1021/acsomega.9b04126.**

65. J., Goel., K., Kadirvelu., C., Rajagopal., and V. K., Garg. (2005). Removal of Lead (II) from Aqueous Solution by Adsorption on Carbon Aerogel Using a Response Surface Methodological Approach, **no. Ii, pp. 1987–1994.**

66. **Y., Wang., L. Li., C., Luo., X., Wang., and H., Duan. (2016).** International Journal of Biological Macromolecules Removal of Pb^{2+} from water environment using a novel magnetic chitosan / graphene oxide imprinted Pb^{2+}, Int. J. Biol. Macromol., **vol. 86, pp. 505–511, doi: 10.1016/j.ijbiomac.2016.01.035.**

67. **Z., Li., Y., Kong., and Y., Ge. (2015).** Synthesis of porous lignin xanthate resin for Pb 2 + removal from aqueous solution, Chem. Eng. J., **vol. 270, pp. 229–234, doi: 10.1016/j.cej.2015.01.123.**

68. **C., Tamez., R., Hernandez., and J. G., Parsons. (2016).** Removal of Cu (II) and Pb (II) from aqueous solution using engineered iron oxide nanoparticles, Microchem. J., **vol. 125, pp. 97–104, doi: 10.1016/j.microc.2015.10.028.**

69. **Y. J., Tu., C. F., You., and C. K., Chang. (2012).** Kinetics and thermodynamics of adsorption for Cd on green manufactured nano-particles, J. Hazard. Mater., **vol. 235–236, pp. 116–122, doi: 10.1016/j.jhazmat.2012.07.030.**

70. **D., Mohan., and K. P., Singh. (2002).** Single- and multi-component adsorption of cadmium and zinc using activated carbon derived from bagasse - An agricultural waste, Water Res., **vol. 36, no. 9, pp. 2304–2318, , doi: 10.1016/S0043-1354(01)00447-X.**

71. **M. M., Rao., A., Ramesh., G. P., Chandra., and K., Seshaiah. (2006).** Removal of copper and cadmium from the aqueous solutions by activated carbon derived from Ceiba pentandra hulls, **vol. 129, pp. 123–129, doi: 10.1016/j.jhazmat.2005.08.018.**

72. **F., Ge., M., Li., H. Ye., and B., Zhao. (2012).** Effective removal of heavy metal ions Cd^{2+}, Zn^{2+}, Pb^{2+}, Cu^{2+} from aqueous solution by polymer-modified magnetic nanoparticles, J. Hazard. Mater., **vol. 211–212, pp. 366–372, , doi: 10.1016/j.jhazmat.2011.12.013.**

73. **J. H., Deng., X. R., Zhang., G. M., Zeng., J. L., Gong., Q. Y., Niu., and J., Liang. (2013).** Simultaneous removal of Cd(II) and ionic dyes from aqueous solution using magnetic graphene oxide nanocomposite as an adsorbent, Chem. Eng. J., **vol. 226, pp. 189–200, doi: 10.1016/j.cej.2013.04.045.**

74. **L., Khezami., K. K., Taha., and O. M., Lemine. (2017).** Uncorrected Proof Uncorrected Proof, **pp. 1–11, doi: 10.2166/aqua.2017.033.**

75. **I., Mobasherpour., E., Salahi., and M., Pazouki. (2011).** Removal of divalent cadmium cations by means of synthetic nano crystallite hydroxyapatite, Desalination, **vol. 266, no. 1–3, pp. 142–148, doi: 10.1016/j.desal.2010.08.016.**

76. **H., Naeem., M., Ajmal., R. B., Qureshi., S. T., Muntha., M., Farooq., and M., Siddiq. (2019).** Facile synthesis of graphene oxide–silver nanocomposite for decontamination of water from multiple pollutants by adsorption, catalysis and antibacterial activity, J. Environ. Manage., **vol. 230, no. June 2018, pp. 199–211, doi: 10.1016/j.jenvman.2018.09.061.**

77. **K., Anandalakshmi. (2021).** Green synthesis, characterization and antibacterial activity of silver nanoparticles using chenopodium album leaf extract," Indian J. Pure Appl. Phys., **vol. 59, no. 6, pp. 456–461, doi: 10.56042/ijpap.v59i6.32055.**

78. **D., Gheidari., M., Mehrdad., S., Maleki., and S., Hosseini. (2020).** Synthesis and potent antimicrobial activity of $CoFe_2O_4$ nanoparticles under visible light, Heliyon, **vol. 6, no. 10, p. e05058, doi: 10.1016/j.heliyon.2020.e05058.**

79. **A., Khan., D., Shabir., P., Ahmad., M. U., Khandaker., M. R. I., Faruque., and I. U., Din. (2021).** Biosynthesis and antibacterial activity of MgO-NPs produced from Camellia-sinensis leaves extract, Mater. Res. Express, **vol. 8, no. 1, , doi: 10.1088/2053-1591/abd421.**